Received: 10 February 2021 | Revised: 8 April 2021 | Accepted: 29 April 2021

IET Microwaves, Antennas & Propagation

DOI: 10.1049/mia2.12161

The Institution of Engineering and Technology WILEY

ORIGINAL RESEARCH PAPER

Evaluation of the E-polarization focusing ability in Thz range for microsize cylindrical parabolic reflector made of thin dielectric layer sandwiched between graphene

Taner Oğuzer[1] | **Ayhan Altıntaş**[2]

[1]Electrical and Electronics Engineering Deparment, Dokuz Eylul University, Buca, Izmir, Turkey

[2]Electrical and Electronics Engineering Department, Bilkent University, Ankara, Turkey

Correspondence

Taner Oğuzer, Electrical and Electronics Engineering Deparment, Dokuz Eylul University, Buca, 35160 Izmir, Turkey.
Email: taner.oguzer@deu.edu.tr

Abstract

We consider two-dimensional (2-D) thin dielectric parabolic reflector, covered with graphene from both sides, illuminated symmetrically by an E-polarized electromagnetic plane wave. Our aim is to estimate the focussing ability of such a composite reflector depending on the graphene parameters. We use a version of the two-side generalized boundary condition, modified for a thin multilayer case. The scattering is formulated as an electromagnetic boundary-value problem; it is cast to a set of two coupled singular integral equations that are further subjected to analytical regularisation based on the known Riemann–Hilbert problem solution. Thanks to this procedure, the numerical results are computed from a Fredholm second-kind matrix equation that guarantees convergence and provides easily controlled accuracy. In the lower part of the THz range, high values of the focusing ability are observed even for a thin reflector; they are greater than for a purely dielectric reflector and a free standing graphene reflector. On the other hand, a regime of almost full transparency, intrinsic for the dielectric layer, can spoil focusing ability. Novel aspect is that the location in frequency of this effect can be controlled, in wide range, by changing the chemical potential of graphene.

1 | INTRODUCTION

Graphene is a very thin material with has special properties like high conductivity, mechanical strength, and optical transparency [1, 2]. It can be used within a wide range of frequencies, from infrared for nanosize samples to THz for microsize samples. In the transverse polarization, it supports the Surface Plasmon (SP) guided wave, and this SP wave produces standing wave pattern on a finite-size scatterer due to the Fabry–Perot type reflection from the edges, in the infrared for nanosize samples and in the THz range for microsize ones. For a graphene sample, the edge effects can be ignored if its size is larger than the 100 nm; hence, in the THz range, for microsize samples one can disregard these edge effects.

Perhaps the most attractive feature of graphene is that its electron conductivity can be adjusted by applying an external biasing electric field, which changes graphene's chemical potential. This promises multiple potential applications of graphene in tuneable sensors, waveguides, and antennas [1].

For the purpose of modelling, the frequency-dependent conductivity of the graphene can be modelled using the Kubo formalism, as explained in [3]. Then, the scattering from a flat or curved graphene strip can be simulated using the electromagnetic boundary-value problem (BVP) with the resistive-sheet boundary condition [3, 4]. For instance, the method of moments (MoM) can be used to treat the singular integral equations (SIEs) obtained from the boundary conditions. However, the accuracy of conventional MoM with sub-domain basis and testing functions is limited to only 2-3 digits. The reason of limited accuracy and generally questionable convergence with denser meshing are related to the singularities of SIE kernels. As a result, only medium-size strips of 10 wavelengths or less can be simulated even with such accuracy. For larger geometries, the MoM matrix grows quickly, and the condition number of the matrix increases. The consequence of this situation is a huge computation time with degrading accuracy. To alleviate this trouble, certain special iterative algorithms are applied to the MoM procedure like fast-multipole

technique and numerical preconditioning. However, this is not easy and convergence is still not guaranteed mathematically, and accuracy suffers, too.

To obtain a more reliable solution of the scattering from a graphene strip, a Nystrom method is used in [5, 6] to discretise the associated SIE, with special quadrature formulas to handle the singularity of the kernels properly. The numerical simulations show that the scattering and absorption parameters are produced with controlled accuracy, and the SP resonances are observed as expected, in the H-polarisation case. The convergence is guaranteed by the theorems of approximation of singular integrals with quadratures [5, 6].

An important alternative is the method of analytical regularization (MAR) [7]. Here, the SIE kernel is separated to two parts, most singular (usually static) and the remainder. The most singular part is analytically inverted using special techniques like the Riemann–Hilbert problem (RHP) method [8–10] or the Abel integral equation method [11, 12], or Galerkin MoM with weighted Chebyshev polynomials which are orthogonal eigenfunctions of the static part [13–15]. The remainder produces a Fredholm second-kind matrix equation, and in this case, the numerical solution is convergent. The SIE–MAR technique enables an accurate and economical solution of the electromagnetic scattering from even quasi-optical size scatterers. For instance, in [16, 17], an arbitrary conic section profile 2-D reflector with a resistive boundary condition is modelled by using RHP based MAR approach, in both polarizations. Infinite graphene-strip grating in the free space was also studied by the MAR–RHP in [9]. In [18], a 2-D parabolic graphene reflector in the free space is modelled using MAR–RHP in the H-polarization case and inverse Fourier transform in the E-case. The SP-wave resonances are observed in H-wave scattering and absorption, and also the focusing ability (FA) is studied as a function of the parameters. The main observation in these studies is that FA increases with larger values for the chemical potential of graphene that translates to the surface reflectivity. However, a graphene reflector in the free space is not a sufficiently realistic model because a control mechanism of the dc biasing is required to adjust the chemical potential of the graphene [2].

In the present study, the scattering and absorption cross-sections (ACSs) and FA are analyzed in the E-polarization case for a thin parabolic dielectric reflector covered with graphene layers from both sides. Our main interest is in the comparison of how the focusing of a THz wave by such a composite reflector can be worse or better than by purely dielectric [19] and purely graphene [18] ones. To model a thin dielectric reflector, in [19] (see also [20]), we use the generalized boundary condition (GBC) with Mitzner [21] and Karlsson [22] type electric and magnetic resistivities on the median line of the reflector. Note that the validity and limitations of such a replacement have been studied in [23]. Further, in [24], the resistivities of a thin dielectric disk sandwiched between two graphene disks have been derived. Using these expressions, we have analyzed, in [25], the scattering of the H-polarized plane wave from a flat dielectric strip covered with graphene, while observing the SP-wave resonances.

The remainder of the present work is as follows. Firstly, the formulation details are explained, and then a set of coupled SIEs for the effective electric and magnetic currents are derived. Their discretization is done similarly to [9, 16–20], and then the numerical results are presented; they cover the frequency dependences of the total scattering and ACSs and FA. Conclusions are summarized in the final section.

2 | SCATTERING PROBLEM FORMULATION

We consider a 2-D reflector as shown in Figure 1 with the aperture dimension denoted as d. We assume that it is made of a dielectric layer with the relative permittivity ε_r and thickness h, sandwiched between two graphene monolayers. The thickness of graphene is implied to be atomically small and ignored, and the thickness of the dielectric is implied to be electrically small, that is, $h << \lambda$. The cross-sectional contour of the reflector has parabolic shape, and f is the focal length. We denote the median line of the reflector crosssection as L.

The reflector explained above is illuminated by the E-polarized plane wave with time dependence $e^{-i\omega t}$ propagating along the positive direction of the x-axis,

$$E_z^{in}(\mathbf{r}) = e^{ikx} \tag{1}$$

The total field is considered as a sum

$$E_z(\mathbf{r}) = E_z^{sc}(\mathbf{r}) + E_z^{in}(\mathbf{r}) \tag{2}$$

where $E_z^{sc}(\mathbf{r})$ is the field scattered by the reflector. Given $E_z(\mathbf{r})$, the other (magnetic) field components can be found from Maxwell equations.

Full-wave formulation of the scattering boundary-value problem for $E_z^{sc}(\mathbf{r})$ demands that it satisfies the Helmholtz equation off L, thin-layer GBC on L, edge condition for the finite local energy in the vicinity of the edge points of M, and Sommerfeld radiation condition. These conditions guarantee the uniqueness of the solution [26].

Considering the GBC on graphene–dielectric–graphene composite, we denote the limiting values of the tangential electric and magnetic field amplitudes from the front (back) side of the reflector as $E_z^{+(-)}(\mathbf{r})$ and $H_T^{+(-)}(\mathbf{r})$, respectively. Then, thanks to the small thickness, the field inside the reflector can be ignored; however, the following GBCs are stated on L [4]:

$$\frac{1}{2}\left[E_z^+(\mathbf{r}) + E_z^-(\mathbf{r})\right] = R^* Z_0 \left[H_T^+(\mathbf{r}) - H_T^-(\mathbf{r})\right] \tag{3}$$

$$\frac{1}{2}\left[H_T^+(\mathbf{r}) + H_T^-(\mathbf{r})\right] = -S^*/Z_0 \left[E_z^+(\mathbf{r}) - E_z^-(\mathbf{r})\right] \tag{4}$$

where R^* and S^* are the dimensionless (i.e. relative) electric and magnetic resistivities, which account for both the effects of the graphene and dielectric layers, and Z_0 is the intrinsic impedance of the free space.

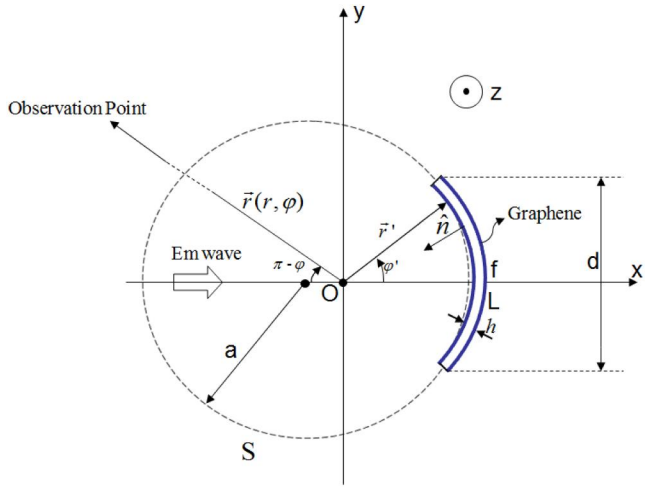

FIGURE 1 Cross-sectional geometry of composite reflector symmetrically illuminated by a plane wave

In general, GBC on a thin composite layer also involves, additionally, a third coefficient called cross-resistivity [4]. However, if the composite has a symmetric arrangement and its radius of curvature is much larger than the thickness (i.e. exactly as in our case), then the cross-resistivity can be neglected [4].

The resistivities, which enter (3) and (4), are empiric values borrowed from the asymptotic analysis of the plane-wave scattering from an infinite flat layer, the thickness of which is much smaller than the free-space wavelength $k_0 h \ll 1$ (the wavelength in the material can be arbitrary) [4]. If the graphene covers are absent and thin non-magnetic dielectric layer has high contrast with the host medium, that is, $|\varepsilon_r| \gg 1$, then the relative electric and magnetic resistivities are found, according to Mitzner [21], as

$$R = \frac{i}{2\sqrt{\varepsilon_r}} \cot\left(\frac{1}{2}\sqrt{\varepsilon_r}\, k_0 h\right) \tag{5}$$

$$S = \frac{i\sqrt{\varepsilon_r}}{2} \cot\left(\frac{1}{2}\sqrt{\varepsilon_r}\, k_0 h\right) \tag{6}$$

Covering the dielectric layer with two graphene covers changes the resistivities of the composite. This is because a monolayer of graphene is an electrically resistive sheet with complex-valued and frequency-dependent resistivity, $R_G = 1/Z_0\sigma$, where σ is the electron conductivity [3]. By following the technique given in [24], one can obtain a GBC for such a composite layer that repeats in the form of equations (3) and (4) but with the following electric and magnetic resistivities:

$$R_{GDG} = \frac{R}{1 + 2Z_0 R\sigma} \tag{7}$$

$$S_{GDG} = Z_0\sigma/2 + S \tag{8}$$

Important for the modelling is the fact that the graphene conductivity has an analytic representation known as Kubo formalism [3]. It has two contributions, called intraband and interband terms, and the intraband term is dominant at all frequencies lower than the visible range; it is also called the Drude-like model—see, for instance, equation 1 of [3].

Although R_{GDG} and S_{GDG} given by (7) and (8) are well-suitable for the modelling of thin composite scatterers, the modelling can be additionally improved using compensation for the layer thickness that happens when we shrink the original layer to its median line.

Following Karlsson [22], the ignored layer thickness can be accounted for via the corresponding phase difference. We then arrive at the following expressions:

$$R^* = \frac{v - R_{GDG} - v^2 R_{GDG}}{4vR_{GDG} - v^2 - 1} \tag{9}$$

$$S^* = \frac{v - S_{GDG} - v^2 S_{GDG}}{4vS_{GDG} - v^2 - 1} \tag{10}$$

where $v = i\cot(k_0 h/4)$, and R_{GDG} and S_{GDG} are given in (7) and (8). Note that if $h \to 0$, then $|v| \to \infty$, and hence, $R^* \to R_{GDG}$ and $S^* \to S_{GDG}$. Therefore, these modified expressions become more important for the thicker layers due to the larger phase correction in comparison with the Mitzner-like ones. Besides, as it is found in [25], the use of the Karlsson correction leads to improvement in the field pattern in the backside region of a thin dielectric reflector.

3 | DERIVATION OF SINGULAR INTEGRAL EQUATIONS AND THEIR DISCRETIZATION WITH MAR

The field scattered by the composite reflector L can be sought as a sum of simple and double-layer potentials, or equivalently, as a sum of convolutions of the effective electric and magnetic surface current densities, $J_z(\mathbf{r}')$ and $M_T(\mathbf{r}')$, with Green's function $G(k_0|\mathbf{r}-\mathbf{r}'|)$ and its normal derivative, respectively. Here, in the E-polarization, J_z is the jump in the tangential H-field, and M_T is the jump in the tangential E-field, across the thin layer of the graphene–dielectric–graphene composite L.

Being substituted into GBC (3) and (4), these integral representations lead to the pair of coupled SIEs for unknown functions J_z and M_T. On extending these functions by zero values to the virtual arc S, which completes the reflector arc L to a closed contour C, we obtain the following pair of coupled dual functional equations:

$$R^* J_z(\mathbf{r}) - ik_0 Z_0 \int_L J_z(\mathbf{r}')\, G(k_0|\mathbf{r}-\mathbf{r}'|)\, dl'$$

$$- \int_L M_T(\mathbf{r}') \frac{\partial}{\partial n'} G(k_0|\mathbf{r}-\mathbf{r}'|)\, dl' = E_z^{in}(\mathbf{r}), \quad \mathbf{r} \in L, \tag{11a}$$

$$J_z(\mathbf{r}) = 0, \quad \mathbf{r} \in S, \tag{11b}$$

and

$$S^* M_T(\mathbf{r}) - \int_L J_z(\mathbf{r}')\, \frac{\partial}{\partial n} G(k_0|\mathbf{r}-\mathbf{r}'|)\, dl'$$

$$- \frac{ik_0}{Z_0} \int_L M_T(\mathbf{r}') \cos[\xi(\mathbf{r}) - \xi(\mathbf{r}')]\, G(k_0|\mathbf{r}-\mathbf{r}'|) dl'$$

$$- \frac{1}{ik_0 Z_0} \int_L M_T(\mathbf{r}')\, \frac{\partial^2}{\partial l\, \partial\, l'} G(k_0|\mathbf{r}-\mathbf{r}'|) dl' = H_T^{in}(\mathbf{r}), \quad \mathbf{r} \in L, \tag{12a}$$

$$M_T(\mathbf{r}) = 0, \quad \mathbf{r} \in S, \tag{12b}$$

where $\xi(\mathbf{r})$ is the angle between the unit normal vector $\hat{n}$ and the x-direction.

Note that the terms containing the normal derivatives of Green's function in the SIE kernels are not singular if their arguments coincide [26]. This means that Equation (11a) has only a logarithmic singularity, associated with the first term. Similar singularity appears in the second term of Equation (12a). However, the third term of that equation has a hyper-type singularity, which is the reason of the absence of convergence if one tries to solve that SIE using conventional MoM with local basis and testing functions. Therefore, to build a convergent numerical code, we need to either use a MAR procedure in combination with a suitable projection scheme or apply a Nystrom-type interpolation with the aid of quadratures. We follow [9, 16–20], where we studied perfect electric conductor (PEC), resistive, thin dielectric, and graphene reflectors, respectively, with the aid of the MAR–RHP scheme.

As explained in [9, 16–20], we have to cast the dual functional Equations (11) and (12) to two coupled dual-series equations and exploit their analytical regularization with the aid of the analytical solution of associated RHP. In this way, we introduce an auxiliary arc S complementing the parabolic arc L to the closed contour C.

To provide a faster convergence of the resulting algorithm, S should be a circular arc of the radius a that equals the radius of the curvature of the parabolic arc L at the endpoints. This ensures that C is a continuous curve with a continuous first derivative, and the second derivative has finite jumps at the junction points. Further, C can be conveniently parametrized in terms of the polar angle ϕ associated with natural coordinates of arc S. The parametric equation of the parabola associated with L can be defined $x = x(\phi), y = y(\phi)$ and can be found in [9, 16–20]. The differential length on L is written as $dl = a\beta(\phi)d\phi$, where $\beta(\phi) = r(\phi)/[a\cos\gamma(\phi)]$, $r(\phi)$ is the angle between the normal to arc L and the x-direction, and $\gamma(\phi)$ is the angle between the normal and radial direction. All these quantities have explicit expressions [9, 16–20].

As J_z and M_T have been extended by zero values to arc S, we can change the domain of integration in (11a) and (12a) to the whole double-smooth contour C and apply the projection of these equations on the set of angular exponents. This yields two coupled dual-series equations (DSE) for the unknown surface current angular Fourier coefficients, namely, $X = \{x_n\}_{n=-\infty}^{+\infty}$ for J_z and $M = \{m_n\}_{n=-\infty}^{+\infty}$ for M_T. Further, the first DSE, generated by (11), can be partially inverted using the inverse Fourier transform. This yields a Fredholm second-kind matrix equation directly, due to the logarithmic-type singularity in the kernel of (11a).

For the second functional equation (12), another Fredholm second-kind matrix equation is obtained after using the RHP method for the analytical inversion of the static part, which contains a hyper-type singularity. The details of this procedure are given in [9, 16–20]. Namely, we add and subtract the auxiliary terms, generated by the Green's function and its derivatives on the circle of radius a, and note that, in the difference term, the singularities of the Green's function on this circle and on L cancel each other. This involves the coefficients of the corresponding double Fourier series for the mentioned functions. Note that the absence of strong singularities and the smoothness of C ensure that these coefficients belong to the l_2 space, and they can be calculated using the fast Fourier transform.

On denoting $Z = \{X, M\}$ and $B = \{E, H\}$, where $E = \{e_n\}_{n=-\infty}^{+\infty}$ and $H = \{h_n\}_{n=-\infty}^{+\infty}$, with e_n and h_n being the Fourier coefficients of the incident field on L, we can write the resulting matrix system as

$$(I - A)Z = B \tag{13}$$

where I is the identity matrix and $A = \{A_{mn}\}_{m,n=-\infty}^{+\infty}$ is a fully populated 2×2 block matrix with elements similar to those in, for example, equations (26) and (27) of [20].

The matrix equation (13) is a Fredholm second-kind equation that follows from the properties $\sum_{m=-\infty}^{\infty} \sum_{n=-\infty}^{\infty} |A_{mn}|^2 < \infty$ and $\sum_{m=-\infty}^{\infty} |B_m|^2 < \infty$, which are established similarly to the dielectric reflector case [19]. Then the Fredholm theorems guarantee that when each block and the right-hand parts are truncated to the finite order N_{tr}, the numerical solutions converge to exact ones at $N_{tr} \to \infty$, and accuracy is controlled by the value of N_{tr}.

4 | SCATTERING AND ABSORPTION CHARACTERISTICS

The scattered field in the far zone of the reflector has the form $E_z^{sc} = \sqrt{2/(i\pi kr)}\, e^{ikr}\, \phi(\varphi)$, where $\phi(\varphi)$ is the angular scattering pattern, which depends on the surface current densities J_z and M_T (see [19] for the corresponding expression).

The total scattering cross-section (TSCS) of the reflector is then found as

$$\sigma_{tsc} = \frac{2}{\pi k_0} \int_0^{2\pi} |\phi(\varphi)|^2 d\varphi \tag{14}$$

In the case of imperfectly conducting reflector, such as graphene or graphene–dielectric composite, another important characteristic is the ACS. The ACS can be obtained either by integration of losses directly or by using the optical theorem. In the latter case, ACS can be found with the following formula:

$$\sigma_{abs} = -4k_0^{-1}\, \mathrm{Re}\phi(0) - \sigma_{tsc} \tag{15}$$

which accounts for the incident plane-wave propagation direction, $\varphi = 0$.

For a parabolic reflector illuminated with a plane wave, TSCS and ACS are useful auxiliary characteristics for better insight into the wave physics. The most important characteristic is related to the near-zone feature, that is, the focusing. FA, in its simplest form, can be defined as the ratio of the magnitude of the total field at the geometrical focus of parabola to the incident field at that point. As in our model, the incident-wave electric field has a unit magnitude value,

$$FA = \left|E_z^{sc}(0,0) + E_z^{in}(0,0)\right| \tag{16}$$

5 | NUMERICAL RESULTS

In this section, we present some results of numerical modelling of the plane-wave scattering and absorption by the considered composite reflector. We have performed our calculations using MATLAB software on a PC with an Intel i7 processor working on the Windows 10 platform. The scattering and absorption characteristics we study are TSCS, ACS, and FA. The relative computational errors related to these values are defined as $\Delta e = |e^{N_{tr}+1} - e^{N_{tr}}| \,/\, |e^{N_{tr}}|$, where '$e$' is taken as one of them. To show the convergence, we compute them as a function of the truncation number, N_{tr}, and plot in semi-logarithmic scale.

Figure 2 shows the typical variation in the relative errors of TSCS and ACS for two different sample frequencies. Note that the both values are computed using far-field data. These plots support the statements on the convergence provided by the use of regularized matrix equation.

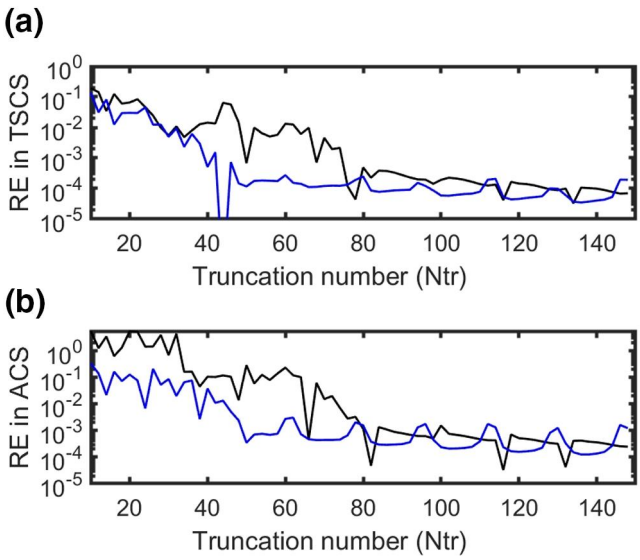

FIGURE 2 The relative error in (a) total scattering cross-section and (b) absorption cross-section for two different frequencies, 4 THz (blue lines) and 7 THz (black lines). The problem parameters are $d = 400$ μm, $f/d = 0.3$, $h = d/400$, $\varepsilon_r = 25 + 0.2i$, and the graphene chemical potential is $\mu_c = 1eV$, $\tau = 1$ ps, and $T = 300$°K

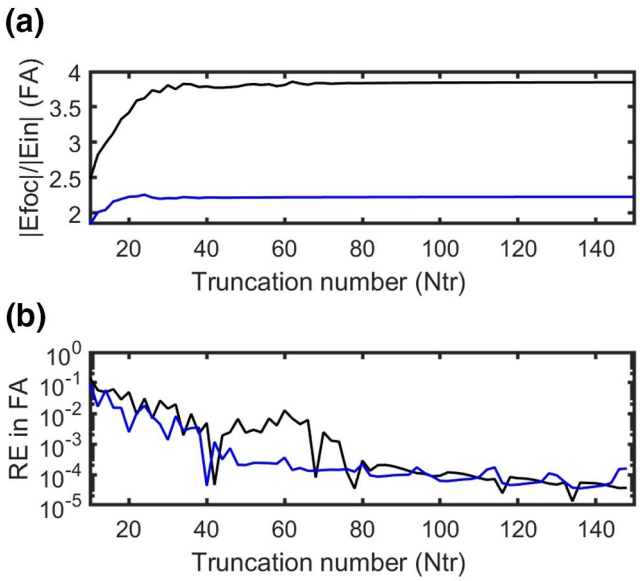

FIGURE 3 (a) Focusing ability (FA) and (b) the relative error in FA for two different frequencies, 4 THz (blue lines) and 7 THz (black lines), versus the matrix truncation number. The problem parameters are $d = 400$ μm, $f/d = 0.3$, $h = d/400$, $\varepsilon_r = 25 + 0.2i$, the graphene chemical potential is $\mu_c = 1$ eV, $\tau = 1$ ps, and $T = 300$°K

Figure 3 shows the variation in FA and its relative error with the increasing N_{tr} at the same two frequencies. As FA can be considered a near-field characteristic of the reflector, which provides a check of the near-field convergence. Both in Figures 2 and 3, the relative error variation has a slowly decaying nature and can be used to estimate the N_{tr} one should take to provide the desired accuracy.

At 7 THz and with the parameters given in Figure 2, the electrical size of the reflector (d/λ) is 9.3. For 10^{-3} relative accuracy, N_{tr} becomes approximately 80. In addition, the memory complexity of the main matrix is 2 $(2N_{tr} + 1) \times 2(2N_{tr} + 1)$, and it has 322 × 322 total elements. Under these conditions, the overall running time is approximately 15 s in MAR with all FFT evaluation and computations of the scattering parameters inside. The memory complexity may be slightly smaller for MoM for the same geometry with the $\lambda/10$ discretization criteria. But one cannot be sure about enough accuracy with this low-level mesh in the conventional MoM. The denser meshing is probably needed, and this will increase the main matrix size. Even in that case, higher accuracy will not be guaranteed. But in MAR, any desired accuracy can be obtained by a sufficiently large increase in the truncation number. Additionally, no integral evaluation is performed in MAR for the main matrix elements, but one can say that double integration will be performed in MoM with the subdomain Galerkin. Therefore, the overall run time will be longer.

The frequency dependences of the scattering and absorption parameters are plotted in Figure 4. Here, the reflector aperture dimension, d, is taken as 400 μm (i.e. 0.4 mm), and the plots are obtained for various layer thicknesses, h. Note that TSCS is roughly by an order of magnitude larger than ACS. Besides, one can notice two distinctive features on these plots.

One is the oscillations within the ACS at higher THz frequencies, especially well visible for thicker reflectors. These oscillations are periodic in frequency and small in magnitude. They are explained by the bouncing of the dielectric-layer guided wave TE_0 between the edges of the reflector, similarly to the same phenomena reported in the E-polarized plane-wave scattering from a flat dielectric strip in [27]. At such high frequencies, graphene is almost transparent because $|R^*| \gg 1$ and its presence has little effect. These resonances make the composite graphene–dielectric–graphene reflector in the E-polarization case similar to the same reflector in the H-polarisation case.

Indeed, in the H-case, the dielectric-layer guided wave TM_0 has its propagation constant very close to k_0 and hence does not lead to standing waves on finite strip. However, in the H-case graphene supports a plasmon guided wave, and, as a result, small periodic resonances should be observed due to bouncing of that wave on graphene covers, similarly to a graphene reflector in the free space [18].

The other feature is the rather deep minimum TSCS at the frequency, which depends on reflector thickness h. These minima are seen at lower frequencies than the frequency of the half-wavelength thickness and depend on the graphene parameters including the chemical potential. They are accompanied with broad peaks of ACS. More precisely, the minimum TSCS occurs around 3.8, 5.2, and 6.4 THz for 2 μm, 1 μm, and 666 nm thicknesses, respectively.

Here, it is useful to compare how this effect appears in the plane-wave scattering from an infinite dielectric slab sandwiched between two graphene sheets. Such a problem can be solved explicitly without the use of GBC using the separation of variables. The corresponding results are shown in Figure 5, where the reflection coefficient is presented in a wide frequency range.

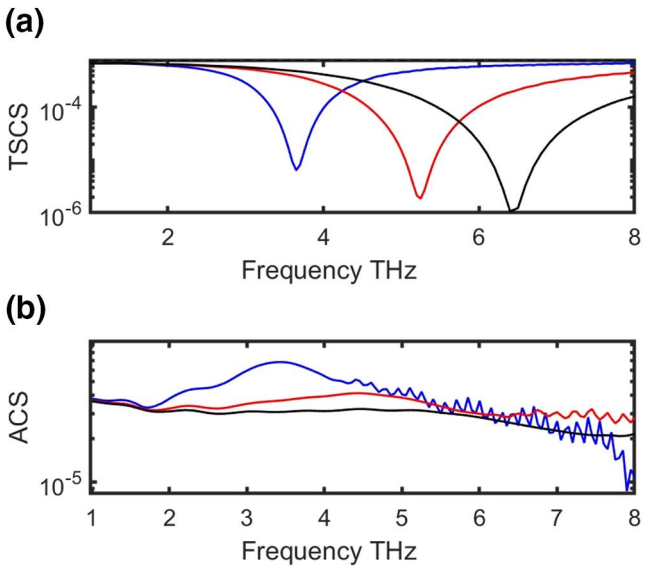

FIGURE 4 (a) Total scattering cross-section (b) absorption cross-section variation with frequency; $h = d/200$ (blue line), $h = d/400$ (red line) and $h = d/600$ (black line). The problem parameters are $d = 400$ μm, $f/d = 0.3$ $\varepsilon_r = 25 + 0.2i$, the graphene chemical potential is $\mu_c = 1$ eV, $\tau = 1$ ps, and $T = 300$°K

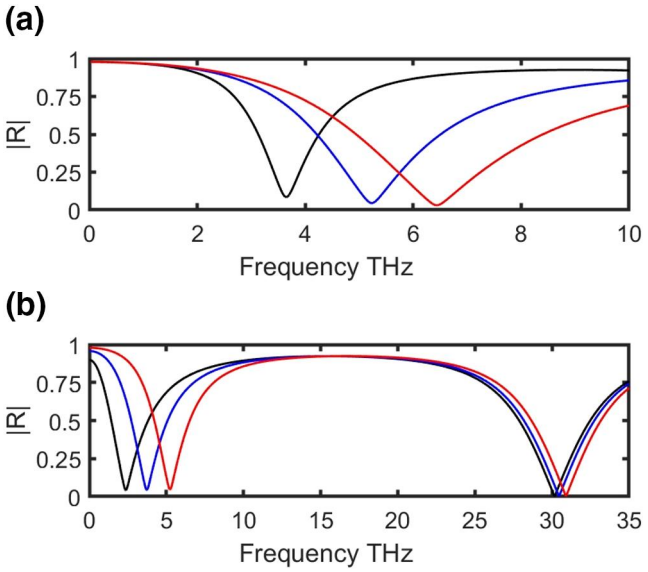

FIGURE 5 The magnitude of the plane-wave reflection coefficient from infinite graphene–dielectric–graphene composite versus the frequency. (a) Reflector thicknesses are $h = d/200$ (black line), $h = d/400$ (blue line), and $h = d/600$ (red line) for graphene chemical potential $\mu_c = 1$ eV. (b) Graphene chemical potentials are $\mu_c = 0.2$ eV(black line), $\mu_c = 0.5$ eV (blue line), and $\mu_c = 1$ eV (red line) for reflector thickness $h = d/400$. The other parameters are $d = 400$ μm, $f/d = 0.3$, and $\varepsilon_r = 25 + 0.2i$, $\tau = 1$ ps, and $T = 300$°K

In Figure 5a, one can see the minima in the reflection coefficient at the same frequencies as in Figure 4a. This agreement can serve as a partial verification of the results computed using GBC. In Figure 5b, the reflection coefficient magnitude is presented within a wider range of frequencies for different chemical potentials of graphene μ_c. As one can see, μ_c can serve as a tool to manipulate the frequency of the minimum reflection (i.e. full transparency) of the composite. From Figure 5b, it can be seen that this occurs only for the first minimum in the low-frequency region. In the second minimum, taking place around 30 THz, all minima are almost at the same frequency. Again, this is because at such high frequencies $|R^*| \gg 1$, graphene is almost transparent, and its presence has little effect.

The frequency scans of FA are presented in Figure 6, where the same quantity computed for the PEC reflector is show for comparison. Note that all curves demonstrate approximately linear growth with frequency because of the growth in the electric size of reflector. This envelope growth, however, is superimposed with oscillations, the period of which is defined by the aperture size, d, in terms of the free-space wavelength, λ_0. This is the result of interference of waves scattered by the edges of the reflector—therefore the period is the same for all curves.

Even though FA for a composite reflector is lower than for a PEC one, they are comparable, and thicker composite reflectors produce larger FA values. What is new, the growth of FA with frequency is spoiled by the total transparency effect, which has been discussed above. The control of the location, in frequency, of this reduction in FA with the aid of the thickness h appears to be impractical for the realization. Therefore, in Figure 7 plot the frequency scans of FA with different values of the chemical potential of the graphene. The plots are obtained for two different thicknesses and the curve for a dielectric reflector without graphene is added for comparison.

One can see that in Figure 7a, which corresponds to a thicker layer, the total transparency regime is reached at the lower frequencies than in Figure 7b, and FA approaches the curve for the dielectric reflector case at high frequencies where graphene becomes transparent. On the other hand, in the lower frequency range in Figure 7b where graphene resistivity is well-conducting, FA shows higher values than for a purely dielectric reflector. The range of almost total transparency is present on all plots except the dielectric reflector case, and its position depends on the chemical potential value, μ_c.

To clarify the dependence of FA on the reflector thickness and graphene potential, we plot it versus h/d and μ_c at the fixed frequency 3 THz in Figure 8a,b, respectively. One can see that the ratio h/d that provides full transparency shifts to smaller values as the chemical potential μ_c gets smaller, and vice versa. Thus, the results shown in Figure 8 certify that FA can be efficiently controlled by using the chemical potential μ_c, which can be adjusted by electrostatic biasing.

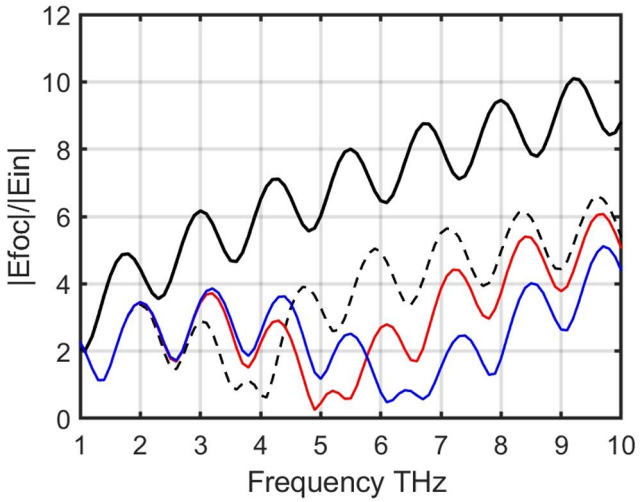

FIGURE 6 The focusing ability variation with frequency. Reflector thickness is $h = d/200$ (dashed line), $h = d/400$ (red line), and $h = d/600$ (blue line); the perfect electric conductor case is shown as a solid black line. The other reflector parameters are $d = 400$ μm, $f/d = 0.3$, and $\varepsilon_r = 25 + 0.2i$. Graphene parameters are $\mu_c = 1$ eV, $\tau = 1$ ps, and $T = 300$°K

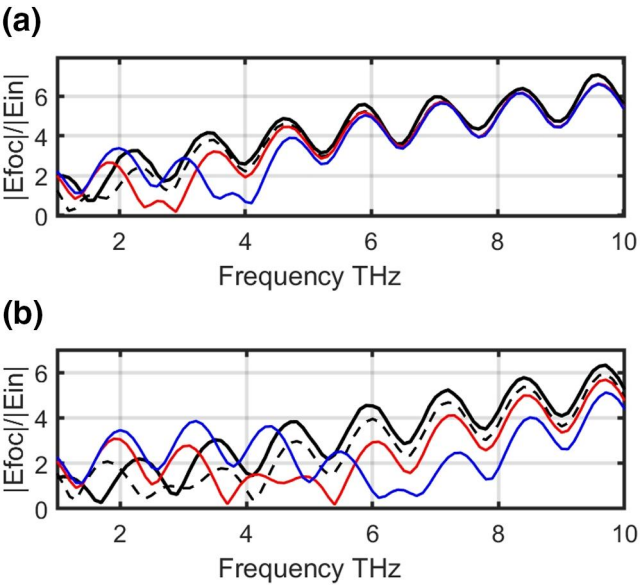

FIGURE 7 The focusing ability variation with frequency for two values of the relative thickness of reflector (a) $h = d/200$ and (b) $h = d/600$. Dielectric reflector case FA is given by the solid black line, the graphene potential is $\mu_c = 0.2$ eV (black dashed line), $\mu_c = 0.5$ eV (red line), and $\mu_c = 1$eV (blue line.) The other parameters are $d = 400$ μm $f/d = 0.3$, $\varepsilon_r = 25 + 0.2i$, $\tau = 1$ ps, and $T = 300$°K

Finally, in Figure 9, we present the total electric field pattern at 7.2 THz around a 0.4 mm reflector that corresponds to $d \approx 10\lambda$. The field magnitude in the geometrical focus is higher than for a free-standing single graphene layer reflector case [18], and fine features of the field are clearly visible

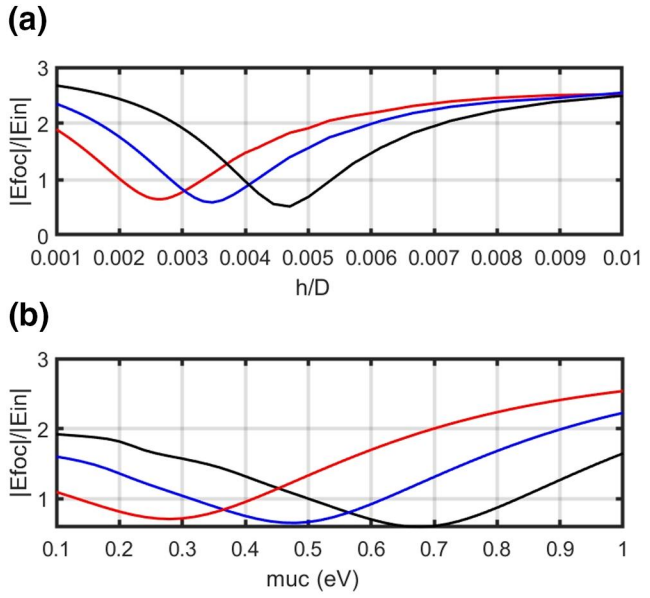

FIGURE 8 (a) The focusing ability variation with h/d (a). Graphene chemical potential is $\mu_c = 0.5$ eV (red line), $\mu_c = 0.7$ eV (blue line), and $\mu_c = 1$ eV (black line) (b) The focusing ability variation with μ_c. Reflector thickness is $h = d/600$ (red line), $h = d/400$ (blue line), and $h = d/300$ (black line). The other parameters are $d = 400$ μm, $f/d = 0.3$, $\varepsilon_r = 25 + 0.2i$, $\tau = 1$ ps, and $T = 300$°K

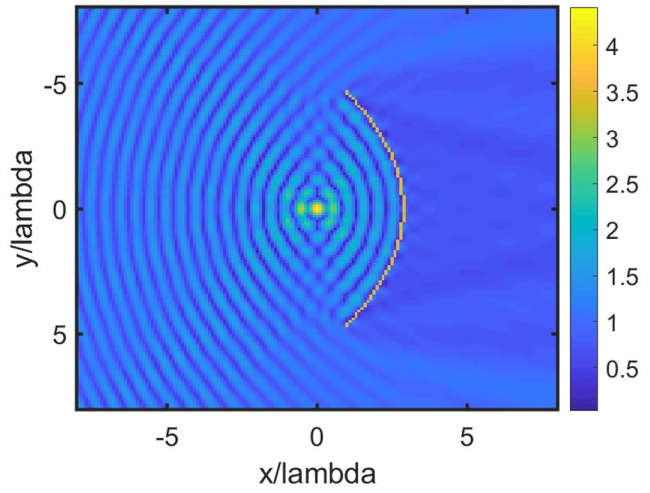

FIGURE 9 The electric field pattern around the composite reflector at 7.2 THz. The problem parameters are $d = 400$ μm, $f/d = 0.3$, $h = d/400$, $\varepsilon_r = 25 + 0.2i$, $\mu_c = 1$ eV, $\tau = 1$ ps, and $T = 300$°K

without any distortion. In Figure 10, we demonstrate an analogous pattern when the frequency is lowered to 4.9 THz so that the electrical size of the reflector reduces to 6.6λ. This frequency corresponds to the regime of almost total transparency of the composite reflector. As expected, the field at focus and in the overall front region is much lower in magnitude than in the previous case, while it is higher at the backside region of the reflector. The observed FA reduction is much greater than the expected drop because of the reduction in d/λ.

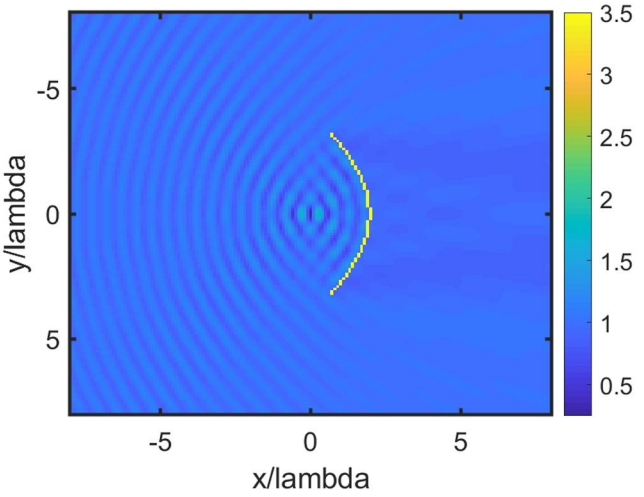

FIGURE 10 The electric field pattern around the composite reflector as in Figure 9 but at 4.9 THz

6 | CONCLUSIONS

We have analyzed the focusing of the E-polarized plane wave by a 2D parabolic reflector made of a thin dielectric layer covered from both sides with graphene monolayers. To reduce the complexity of the scattering problem, we have used two-sided GBCs, which enable us to eliminate the field inside the thin layer from consideration. These conditions lead to a set of coupled SIE for the effective electric and magnetic currents on the composite reflector. We use the MAR approach to build a reliable and economic numerical code where the most singular part of SIEs is inverted analytically based on the known RHP solution. The resulting set of the coupled matrix equations is of the Fredholm second-kind type, and hence the convergence of its solution with larger truncation orders is guaranteed.

In computations, we plotted the frequency dependences of FA, TSCS, and ACS within the entire THz range; only symmetric incidence has been considered. Unlike suspended graphene, the considered geometry is more adequate to real-life situations where a biasing circuit for control of the chemical potential of graphene is needed. As we have found, the field in the geometrical focus of this composite reflector can be considerably higher than for a parabolic reflector made of graphene as studied in [18].

At relatively low frequencies, in the THz range, because of the high conductivity of graphene, the reflectivity of the composite is high. This is completely different from a dielectric slab without graphene and entails higher values of FA. However, at higher THz frequencies, graphene's effect fades off because of its lower conductivity, and as a result, the effect of the dielectric layer becomes dominant. Between these two physical regimes, a region of almost total transparency of the composite can exist where FA drops dramatically. The spectral position of the regime of full transparency of the composite layer depends on the layer thickness similar to the bare dielectric layer. However, and this is perhaps the most

interesting result, we have found that transparency frequency can be tuned within a wide range using the chemical potential of graphene. This situation is observed to be especially clear for relatively thinner composite reflectors.

ORCID

Taner Oğuzer https://orcid.org/0000-0003-1990-4301

REFERENCES

1. Low, T., Avouris, P.: Graphene plasmonics for terahertz to mid-infrared applications. ACS Nano. 8, 1086–1101 (2014)
2. Shukla, S., Kang, S.Y., Saxena, S.: Synthesis and patterning of graphene: strategies and prospects. Appl. Phys. Rev. 6, 021311 (2019)
3. Hanson, G.W.: Dyadic Green's functions and guided surface waves for a surface conductivity model of graphene. J. Appl. Phys. 103, 064302 (2008)
4. Bleszynski, E.H., Bleszynski, M.K., Jaroszewicz, T.: Surface-integral equations for electromagnetic scattering from impenetrable and penetrable sheets. IEEE Antenn. Propag. Mag. 35, 14–25 (1993)
5. Balaban, M.V., Shapoval, O.V., Nosich, A.I.: THz wave scattering by a graphene strip and a disc in the free space: integral equation analysis and surface plasmon resonances. Int J Optics. 15(11), 114007 (2013)
6. Kaliberda, M.E., Lytvynenko, L.M., Pogarsky, S.A.: Modelling of graphene planar grating in the THz range by the method of singular integral equations. Frequenz. 72, 277–284 (2018)
7. Nosich, A.I.: Method of analytical regularization in computational photonics. Radio Sci. 51(8), 1421–1430 (2016)
8. Koshikawa, S., et al.: A comparative study of RCS predictions of canonical rectangular and circular cavities with double-layer material loading. IEICE Trans. Electron. E80-C(11), 1457–1466 (1997)
9. Oguzer, T., Nosich, A.I., Altintas, A.: E-polarized beam scattering by an open cylindrical PEC strip having arbitrary conical-section profile. Microw. Opt. Technol. Lett. 31(6), 480–484 (2001)
10. Zinenko, T.L.: Scattering and absorption of terahertz waves by a free-standing infinite grating of graphene strips: analytical regularization analysis. Int J Optics. 17(5), 055604 (2015)
11. Smith, P.D.: Recent advances in regularization techniques for scattering and diffraction. Radio Sci. 42(6), 1–23 (2007)
12. Vinogradova, E.D., Kobayashi, K., Eizawa, T.: Full wave analysis of plane wave diffraction by a finite sinusoidal grating: E-polarization case. Wave Motion. 86, 44–62 (2019)
13. Rodriguez-Berral, R., et al.: Quasi-analytical modelling of transmission/reflection in strip/slit gratings loaded with dielectric slabs. IEEE Trans. Microw. Theor. Tech. 60(3), 405–418 (2012)
14. Lucido, M., et al.: Efficient evaluation of slowly converging integrals arising from the application of MAP to a spectral domain integral equation, Electronics. 8(12), 1500 (2019)
15. Zinenko, T.L., Matsushima, A., Nosich, A.J.: Terahertz range resonances of metasurface based on double grating of microsize graphene strips inside dielectric slab. Proc. R. Soc. A. 476(2240), 20200173 (2020)
16. Oğuzer, T., Altintas, A., Nosich, A.I.: Integral equation analysis of an arbitrary profile and varying-resistivity cylindrical reflector illuminated by an E-polarized complex source-point beam. J. Opt. Soc. Am. A Opt. Image Sci. Vis. 26, 1525–1532 (2009)
17. Oğuzer, T., Altintas, A., Nosich, A.I.: Analysis of the elliptic-profile cylindrical reflector with a varying resistivity using the complex source and dual-series approach: H-polarization case. Opt. Quant. Electron. 45, 797–812 (2013)
18. Oguzer, T., Altintas, A., Nosich, A.I.: Focussing of THz waves with a microsize parabolic reflector made of graphene in the free space. J. Eur. Opt. Soc. 13, 16 (2017)
19. Oğuzer, T., et al.: Analysis of a thin, penetrable, and non-uniformly loaded cylindrical reflector illuminated by a complex line source. IET Microw. Antennas Propag. 11(15), 2148–2154 (2017)
20. Kuyucuoglu, F., et al.: Analysis of an arbitrary-profile, cylindrical, impedance reflector surface illuminated by an E-polarized complex line source beam. J. Electromagn. Waves Appl. 28(3), 360–377 (2014)
21. Mitzner, K.: Effective boundary conditions for reflection and transmission by an absorbing shell of arbitrary shape. IEEE Trans. Antenn. Propag. 16, 706–712 (1968)
22. Karlsson, A.: Approximate boundary conditions for thin structures. IEEE Trans. Antenn. Propag. 57(1), 144–148 (2009)
23. Sukharevsky, I.O., et al.: Validity and limitations of the median-line integral equation technique in the scattering by material strips of subwavelength thickness. IEEE Trans. Antenn. Propag. 62(7), 3523–3631 (2014)
24. Balaban, M.V.: Modelling of stratified graphene-dielectric structures using the generalized boundary conditions: THz wave scattering by a thin sandwiched disk. Proceeding of the International Conference on Electronics and Nanotechnology (ELNANO-2015), 207–210 (2015)
25. Oguzer, T., Altintas, A.: Electromagnetic scattering of THz waves from a microsize graphene-sandwiched thin dielectric strip. Proceedings of the International Conference on Mathematical Methods in Electromagnetic Theory (MMET-2018), 91–94 (2018)
26. Colton, D., Kress, R.: Integral Equation Method in Scattering Theory. Wiley (1983)
27. Shapoval, O.V., Sauleau, R., Nosich, A.I.: Fabry-Perot-like resonances in the E-polarized electromagnetic plane wave scattering and absorption by a thin dielectric strip. Proceeding of the European Conference on Antennas and Propagation (EuCAP-2012), Pragueart. no A07-2.3 (2012)

How to cite this article: Oğuzer, T., Altıntaş, A.: Evaluation of the E-polarization focusing ability in Thz range for microsize cylindrical parabolic reflector made of thin dielectric layer sandwiched between graphene. IET Microw. Antennas Propag. 15(10), 1240–1248 (2021). https://doi.org/10.1049/mia2.12161